European Radiology
https://doi.org/10.1007/s00330-023-10215-z

European Radiology
EUROPEAN SOCIETY OF RADIOLOGY

NEURO

Simultaneous quantification of perfusion, permeability, and leakage effects in brain gliomas using dynamic spin-and-gradient-echo echoplanar imaging MRI

Francesco Sanvito[1,2,3] · Catalina Raymond[1,2] · Nicholas S. Cho[1,2,4,5] · Jingwen Yao[1,2] · Akifumi Hagiwara[1,2,6] · Joey Orpilla[7] · Linda M. Liau[7] · Richard G. Everson[7] · Phioanh L. Nghiemphu[8] · Albert Lai[8] · Robert Prins[7] · Noriko Salamon[2] · Timothy F. Cloughesy[8] · Benjamin M. Ellingson[1,2,4,5,7,9]

Received: 13 April 2023 / Revised: 5 July 2023 / Accepted: 27 July 2023

Abstract

Objective To determine the feasibility and biologic correlations of dynamic susceptibility contrast (DSC), dynamic contrast enhanced (DCE), and quantitative maps derived from contrast leakage effects obtained simultaneously in gliomas using dynamic spin-and-gradient-echo echoplanar imaging (dynamic SAGE-EPI) during a single contrast injection.

Materials and methods Thirty-eight patients with enhancing brain gliomas were prospectively imaged with dynamic SAGE-EPI, which was processed to compute traditional DSC metrics (normalized relative cerebral blood flow [nrCBV], percentage of signal recovery [PSR]), DCE metrics (volume transfer constant [K^{trans}], extravascular compartment [v_e]), and leakage effect metrics: $\Delta R_{2,ss}$* (reflecting T_2*-leakage effects), $\Delta R_{1,ss}$ (reflecting T_1-leakage effects), and the transverse relaxivity at tracer equilibrium (*TRATE*, reflecting the balance between $\Delta R_{2,ss}$* and $\Delta R_{1,ss}$). These metrics were compared between patient subgroups (treatment-naïve [TN] vs recurrent [R]) and biological features (IDH status, Ki67 expression).

Results In IDH wild-type gliomas (IDH^{wt}—i.e., glioblastomas), previous exposure to treatment determined lower TRATE ($p = 0.002$), as well as higher PSR ($p = 0.006$), K^{trans} ($p = 0.17$), $\Delta R_{1,ss}$ ($p = 0.035$), v_e ($p = 0.006$), and ADC ($p = 0.016$). In IDH-mutant gliomas (IDH^{m}), previous treatment determined higher K^{trans} and $\Delta R_{1,ss}$ ($p = 0.026$). In TN-gliomas, dynamic SAGE-EPI metrics tended to be influenced by IDH status (p ranging 0.09–0.14). *TRATE* values above 142 $mM^{-1}s^{-1}$ were exclusively seen in TN-IDH^{wt}, and, in TN-gliomas, this cutoff had 89% sensitivity and 80% specificity as a predictor of Ki67 > 10%.

Conclusions Dynamic SAGE-EPI enables *simultaneous* quantification of brain tumor perfusion and permeability, as well as mapping of novel metrics related to cytoarchitecture (*TRATE*) and blood–brain barrier disruption ($\Delta R_{1,ss}$), with a single contrast injection.

Clinical relevance statement Simultaneous DSC and DCE analysis with dynamic SAGE-EPI reduces scanning time and contrast dose, respectively alleviating concerns about imaging protocol length and gadolinium adverse effects and accumulation, while providing novel leakage effect metrics reflecting blood–brain barrier disruption and tumor tissue cytoarchitecture.

Key Points

- *Traditionally, perfusion and permeability imaging for brain tumors requires two separate contrast injections and acquisitions.*
- *Dynamic spin-and-gradient-echo echoplanar imaging enables simultaneous perfusion and permeability imaging.*
- *Dynamic spin-and-gradient-echo echoplanar imaging provides new image contrasts reflecting blood–brain barrier disruption and cytoarchitecture characteristics.*

Extended author information available on the last page of the article

Published online: 26 October 2023

Graphical Abstract

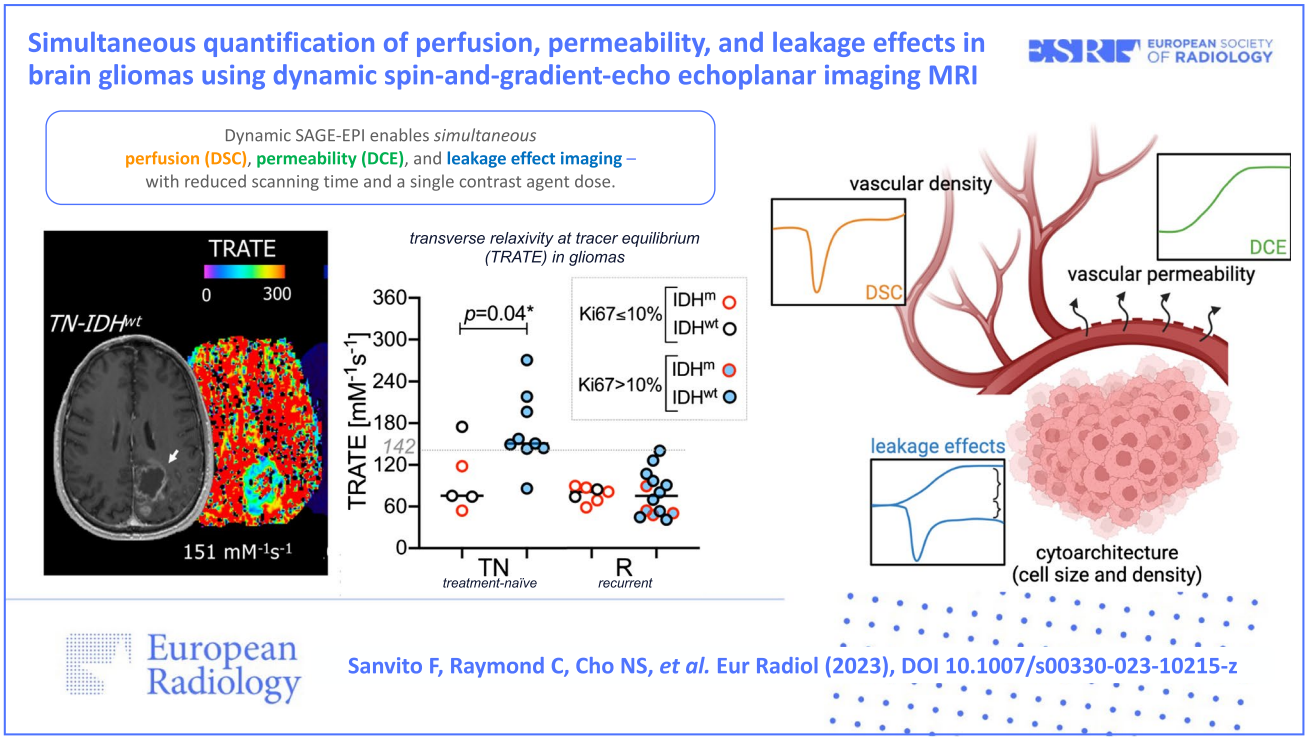

Keywords Glioblastoma · Magnetic resonance imaging · Perfusion imaging · Vascular permeability · Blood–brain barrier

Abbreviations

ADC	Apparent diffusion coefficient
AIF	Arterial input function
BBB	Blood–brain barrier
CA	Contrast agent
DCE	Dynamic contrast enhanced
DSC	Dynamic susceptibility contrast
DTI	Diffusion tensor imaging
DWI	Diffusion-weighted imaging
E1	Echo 1 of dynamic SAGE-EPI
E2	Echo 2 of dynamic SAGE-EPI
EEC	Extravascular extracellular space
EIC	Extravascular intracellular space
FA	Flip angle
FLAIR	Fluid-attenuated inversion recovery
GE	Gradient echo
IDH	Isocitrate dehydrogenase
IDH^{m}	IDH-mutant
IDH^{wt}	IDH wild-type
IV	Intravascular space
K^{trans}	Volume transfer constant
MRI	Magnetic resonance imaging
nrCBV	Normalized relative cerebral blood volume
PSR	Percentage of signal recovery
R	Recurrent
ROI	Region of interest
SAGE-EPI	Spin-and-gradient-echo echoplanar imaging
TE	Echo time
TN	Treatment-naïve
TR	Repetition time
TRATE	Transverse relaxation at tracer equilibrium
v_e	Extravascular compartment
$\Delta R_{1,ss}$	Change in longitudinal relaxation rate over time compared to baseline
$\Delta R_{2,ss}^{*}$	Change in transverse relaxation rate over time compared to baseline

Introduction

Brain gliomas are characterized by heterogeneous prognosis, depending on biological and molecular features [1, 2] and on a variable response to treatment [3–5]. Aggressive tumors rely on a more intense neoangiogenesis, resulting in a dysfunctional neovasculature with blood–brain barrier (BBB) breakdown [6–9]. Magnetic resonance imaging (MRI) can non-invasively quantify vascularization and BBB permeability in vivo, using two separate techniques based on contrast agent (CA) administration: dynamic susceptibility contrast (DSC), a T_2*-weighted gradient-echo (GE) sequence, and

dynamic contrast enhanced (DCE), a T_1-weighted sequence [10]. While DSC perfusion imaging yields rCBV (relative cerebral blood volume), reflecting vascular density [11], DCE permeability imaging allows to compute K^{trans} (volume transfer constant), representing the rate of CA leakage and therefore BBB permeability [12]. These techniques can aid glioma grading [13–15], molecular profiling [16–19], differential diagnosis [10, 20–24], and the distinction between treatment effects and tumor recurrence [10, 24–27], and have become part of the clinical brain tumor work-up in many neuroimaging centers [28]. However, performing perfusion (DSC) and permeability (DCE) imaging requires two separate acquisitions, which increases scanning time, and two full CA doses, which raises concerns for chronic gadolinium deposition [29] and adverse effects in patients with impaired renal function [30].

Dual-echo DSC simultaneously acquires two GE echoes, which can be processed to disentangle the T_2*- and T_1-contributions that coexist in a DSC sequence [31]. In fact, DSC bears some T_1-weighting, which can be sorted out by analyzing two GE echoes. The T_1-contribution can further be used for a DCE analysis, enabling complementary permeability imaging without extra scanning time and without a second CA dose [31].

Additionally, dual-echo DSC allows to compute quantitative maps derived from CA leakage effects. In the presence of BBB breakdown, CA leaks from the intravascular (IV) to the extravascular extracellular (EEC) compartment, resulting in competing T_2*- and T_1-leakage effects, whose balance is influenced by tissue-related factors [32, 33]. In a traditional single-echo DSC, the overall balance between T_2*- and T_1-leakage effects can be evaluated with a metric named percentage of signal recovery (PSR) [34], which is valuable for differential diagnosis because tissue-related factors differ among tumor types (gliomas, lymphomas, and meningiomas) [34, 35]. However, PSR strongly depends on acquisition parameters such as flip angle (FA) and echo time (TE) [36], a major obstacle when generalizing reliable PSR cutoffs across institutions. Moreover, PSR only provides overall estimates of the balance between T_2*- and T_1-leakage effects, which cannot be disentangled with a single-echo DSC. Conversely, dual-echo DSC allows to *separately* evaluate T_1 and T_2* contributions, and to compute a novel quantitative biomarker named transverse relaxivity at tracer equilibrium (*TRATE*), which quantifies T_2*-leakage effects normalized to the estimated CA concentration (derived from T_1-leakage effects) [32, 33]. Despite bearing similar information to PSR, *TRATE* is independent from acquisition factors (FA and TE) [33]. Results from simulated and preclinical data advocate for *TRATE* as a biomarker for cytoarchitectural features such as cell volume fraction and cell size, but its application on human brain tumors has only been preliminary explored in five recurrent high-grade gliomas [33].

In this study, we aim to *simultaneously* obtain perfusion, permeability, and novel leakage effect maps in a cohort of human gliomas, both newly diagnosed and recurrent, using a dynamic spin-and-gradient-echo echo-planar imaging (dynamic SAGE-EPI) acquisition. In fact, the first and second echoes of a dynamic SAGE-EPI can serve as a dual-echo DSC sequence. First, we hypothesize that *TRATE* will correlate with PSR, and that $\Delta R_{1,ss}$ (quantifying T_1-leakage effects) will correlate with K^{trans}, since these metrics are considered quantitative markers for cytoarchitecture (*TRATE* and PSR) and BBB permeability ($\Delta R_{1,ss}$ and K^{trans}), respectively. Second, we hypothesize that increased *TRATE* will reflect aggressive cytoarchitectural features, and will therefore be higher in tumors with higher expression of Ki67 (a marker of cell proliferation) and with IDH wild-type (IDH^{wt}) status (i.e., glioblastomas).

Materials and methods

Patient selection

Patients who gave informed written consent to join the research studies approved by our institutional review board (IRB#14-001261 and #21-000514) were imaged prospectively at our institution. At the time of the study, IRB#14-001261 included patients acquired from April 2015 to October 2020, while IRB#21-000514 from October 2021 to June 2022. Inclusion criteria for the present study were as follows: enhancing lesion, availability of dynamic SAGE-EPI datasets, surgical resection *after* dynamic SAGE-EPI, availability of surgical pathological reports, histopathological diagnosis of adult-type diffuse glioma (i.e., astrocytoma, oligodendroglioma, or glioblastoma) [1].

Magnetic resonance imaging

Magnetic resonance imaging data was collected using a 3-T Siemens Prisma (Siemens Healthineers) according to the standardized brain tumor imaging protocol [37], including pre- and post-contrast T_1-weighted images at 1-mm isotropic resolution, T_2-weighted FLAIR images with 3-mm slice thickness, diffusion tensor imaging (DTI) with 2-mm isotropic resolution obtained in 64 directions with *b*-values = 1000 s/mm^2, and a single $b = 0$ image. The apparent diffusion coefficient (ADC) was estimated from the mean diffusivity computed from the DTI tensor on the scanner. A custom dynamic SAGE-EPI sequence (patent: US 11,378,638 B2) [11, 38, 39] was acquired during injection of a single dose of Gadavist® (Gadobutrol, Bayer) (~ 0.1 mL/kg) at a rate of

~ 4 mL/s, according to guidelines [40]. Dynamic SAGE-EPI was acquired using two gradient echoes (echo 1 with TE_1 = 14 ms, echo 2 with TE_2 = 34.1 ms), an asymmetric spin echo (TE_3 = 58.0 ms), and a spin echo (TE_4 = 92.4 ms), with a repetition time (TR) = 2000 ms, matrix size = 240 × 218 mm, GRAPPA = 3, voxel size 1.875 × 1.875 × 5 mm, 19 axial slices, and 90 repetitions.

Image analysis

Dynamic SAGE-EPI was processed according to the pipeline in Fig. 1. The first GE (echo 1: E1) and second GE (echo 2: E2) were separated, and motion-corrected using FSL (University of Oxford, https://fsl.fmrib.ox.ac.uk/fsl/) *mcflirt* function. The changes in transverse relaxation rate over time compared to baseline ($\Delta R_2^*(t)$ curve, [s^{-1}]), quantifying T_2*-contribution (Suppl. Eq. 1), and T_1-contribution over time ($T_1w(t)$) [arbitrary units] (Suppl. Eq. 2) were obtained voxel-wise as illustrated in Stokes et al [31], where $T_1w(t)$ is the extrapolated signal for TE = 0 ms. For visualization, $\Delta T_2^*(t)$ [s] and $\Delta T_1w(t)$ [arbitrary units] curves were also obtained (Suppl. Eq. 3). To quantify T_1 effects, the change in longitudinal relaxation rate over time compared to baseline ($\Delta R_1(t)$ curve, [s^{-1}]) was computed on a voxel-wise basis from $T_1w(t)$ according to the equations from the Quantitative Imaging Biomarkers Alliance (QIBA, https://www.rsna.org/research/quantitative-imaging-biomarkers-alliance), assuming a fixed T_1 (T_{10}) of 1.4s for tissue, as proposed in Conte et al [41] (Suppl. Eq. 4). An estimated CA concentration over time (C(t)) [mM^{-1}] was obtained by normalizing $\Delta R_{1,ss}$ to the longitudinal relaxivity of Gadobutrol at 3T (r_1), set to 5.0 $mM^{-1}s^{-1}$ as computed by Rohrer et al [42] (Suppl. Eq. 5) and reported by the American College of Radiology (https://www.acr.org).

$\Delta R_{2,ss}$* (ΔR_2* at steady state), $\Delta R_{1,ss}$ (ΔR_1 at steady state), and C_{ss} (CA concentration at steady state) voxel-wise maps were computed by averaging the final 10 time-points of the $\Delta R_2^*(t)$, $\Delta R_1(t)$, and $C(t)$ time curves, respectively [33]. $\Delta R_{2,ss}$* and C_{ss} were combined to compute

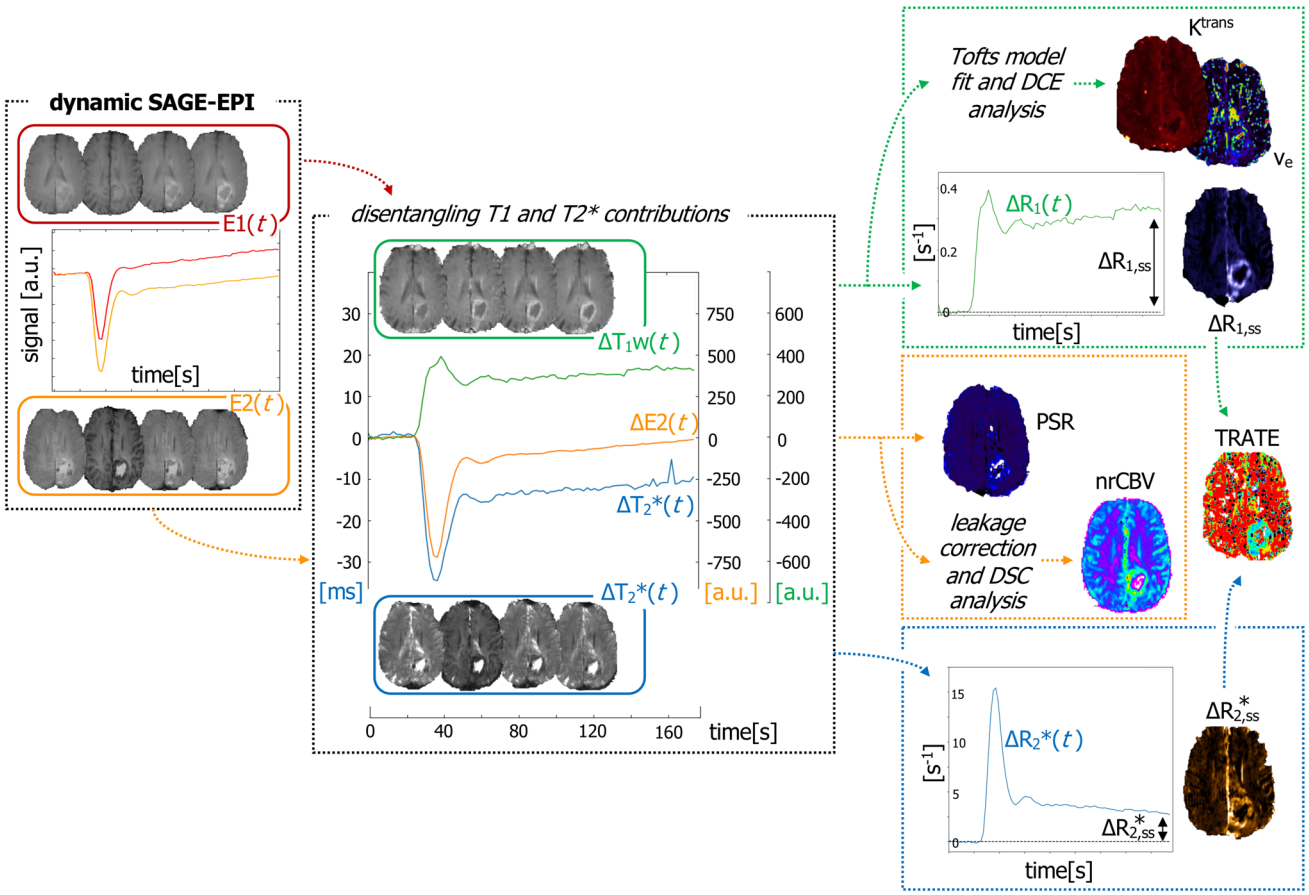

Fig. 1 Image processing pipeline of dynamic SAGE-EPI to obtain MRI quantitative maps. From echo 1 (E1, red, a GE with TE = 14 ms) and echo 2 (E2, orange, a GE with TE = 34.1 ms) of the dynamic SAGE-EPI datasets, the T_1 (green) and T_2* (blue) contributions to DSC signals were disentangled. The T_1 contribution was used for DCE analysis and to quantify $\Delta R_{1,ss}$, while the T_2* contribution was used to quantify $\Delta R_{2,ss}$*. *TRATE* was generated from $\Delta R_{2,ss}$* and $\Delta R_{1,ss}$. The classic DSC metrics were computed from E2

the transverse relaxivity at tracer equilibrium (*TRATE* [$mM^{-1}s^{-1}$]), corresponding to T_2*-leakage effects normalized to CA concentration (Suppl. Eq. 5) [33]. *TRATE*, $\Delta R_{2,ss}$*, and $\Delta R_{1,ss}$ will be referred to as "leakage effect maps."

Normalized rCBV maps (nrCBV) were generated from E2 with a bidirectional leakage correction algorithm [43] with subsequent normalization to the cerebral median rCBV. PSR maps were generated from E2 without leakage correction, as described in Lee et al [35].

For DCE analysis, a Tofts model [12] was fit to $T_1w(t)$ (assuming T_{10} and r_1 as above) to compute voxel-wise K^{trans} and v_e (extracellular volume) maps, by adapting the open-access OSIPI DCE code (https://osipi.org/). A region of interest (ROI) was placed in the superior sagittal sinus to extract the arterial input function (AIF). Unlike DSC, the proposed DCE analysis is *not* "traditional," as it is based on $T_1w(t)$ computed from dynamic SAGE-EPI, as opposed to acquired T_1-weighted datasets.

All maps were registered to post-contrast T1 with the FSL *flirt* function.

Segmentation and quality check

Pre- and post-contrast T_1-weighted images were co-registered, normalized, and voxel-by-voxel subtracted to obtain T_1-weighted subtraction maps, as described in Ellingson et al [5]. Voxels with a ≥ 10% increase in normalized T_1 signal after CA administration were isolated within the lesion area and included in the enhancing tumor segmentation. A neuroradiologist with 7 years of experience in neuroimaging (F.S.) quality-checked maps, registrations, segmentations, AIF-ROIs, and Tofts fits.

Clinical and pathological information

The patients' clinical records and pathology reports were reviewed in order to retrieve the following information: sex category, age, previous exposure to treatment, tumor grade and molecular status, Ki67 expression.

Statistical analyses

Median values of MRI metrics were extracted from the tumor segmentation. The linear correlation between continuous variables was assessed with a correlation coefficient, interpreted as in previous literature [44, 45]. Group differences were assessed with Mann-Whitney *U* tests. Ki67 expression was binarized as ≤ 10% or > 10% as validated in previous studies [46, 47]. The significant *p*-value threshold was set to $p < 0.05$.

Results

Patients' cohort characteristics

Thirty-eight patients met the inclusion criteria (Fig. 2): fourteen treatment-naïve (TN) and twenty-four recurrent (R). Demographic, clinical, and pathological features of the cohort are summarized in Table 1. Suppl. Fig. 1 presents an overview of conventional MRI appearances of representative cases with various grades and treatment statuses.

Relationships among MRI metrics

Correlations among MRI metrics are displayed in Table 2 and Fig. 3a.

TRATE values strongly correlated with $\Delta R_{2,ss}$* ($p = 0.004$, $r = +0.71$) but and not with $\Delta R_{1,ss}$ ($p = 0.32$) in TN-gliomas, while moderately correlated with both $\Delta R_{2,ss}$* ($p = 0.02$, $r = +0.46$; Fig. 3a) and $\Delta R_{1,ss}$ ($p = 0.04$, $r = -0.42$) in R-gliomas. *TRATE* values correlated with ADC ($p = 0.04$, $r = -0.54$) and nrCBV ($p = 0.02$, $r = +0.60$) in TN-gliomas, but not in R-gliomas. As expected, *TRATE* strongly correlated with PSR (TN/R: $p < 0.0001/p = 0.0003$, $r = -0.87/r = -0.68$; Fig. 3a).

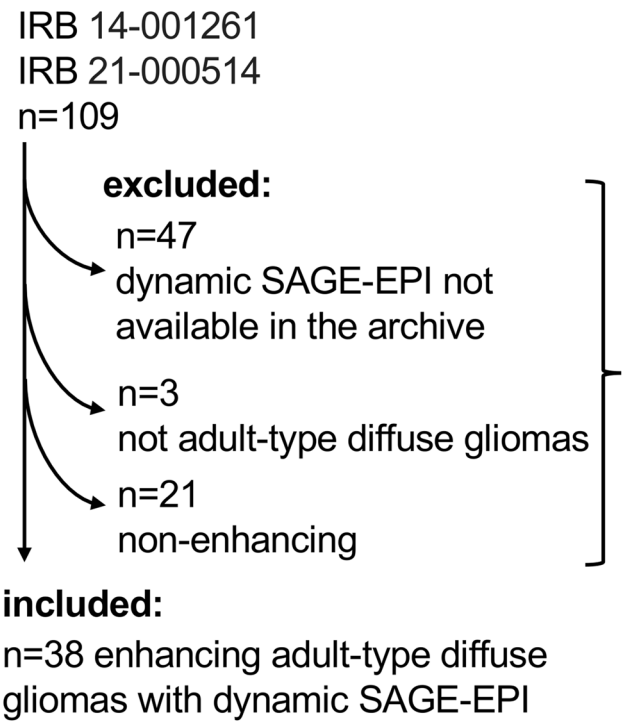

Fig. 2 Flowchart of patients included and excluded from the study

Table 1 Demographic, clinical, and pathological features of the patients' cohort

	Treatment-naïve $n = 14$	Recurrent $n = 24$
Age (years)	61.8 ± 12.9	50.1 ± 13.1
Sex category (F)	4 (28.6%)	7 (29.2%)
Main location		
Frontal	3 (21.4%)	8 (33.3%)
Parietal	3 (21.4%)	5 (20.8%)
Temporal	5 (35.7%)	4 (16.7%)
Multiple lobes	1 (7.1%)	5 (20.8%)
WM/deep GM	2 (14.3%)	2 (8.3%)
Grade		
2	1 (7.1%)	3 (12.5%)
3	1 (7.1%)	3 (12.5%)
4	12 (85.7%)	18 (75%)
Ki67 expression		
≤ 10%	5 (35.7%)	7 (29.2%)
> 10%	9 (64.3%)	14 (58.3%)
Not tested	0 (0%)	3 (12.5%)
IDH and 1p/19q		
IDH^m $1p/19q^{int}$	1 (7.1%)	9 (37.5%)
IDH^m $1p/19q^{cod}$	1 (7.1%)	2 (8.3%)
IDH^{wt}	12 (85.7%)	13 (54.2%)
MGMT promoter		
Methylated (> 2%)	7 (50%)	12 (50%)
Unmethylated	7 (50%)	11 (45.8%)
Not tested	0 (0%)	1 (4.2%)
EGFR		
Amplified	5 (37.5%)	8 (33.3%)
Non-amplified	8 (57.1%)	11 (45.8%)
Not tested	1 (7.1%)	5 (20.8%)

Age is expressed as mean ± standard deviation. *WM*, white matter; *GM*, gray matter; *IDH^m*, IDH-mutant; *IDH^{wt}*, IDH wild-type; *$1p/19q^{cod}$*, 1p/19q codeleted; *$1p/19q^{int}$*, 1p/19q intact

Similarly to *TRATE*, PSR values depended on $\Delta R_{2,ss}$* in both TN- ($p = 0.02$, $r = -0.61$) and R-gliomas ($p = 0.03$, $r = -0.45$), but not on $\Delta R_{1,ss}$. Like *TRATE*, in TN-gliomas, PSR correlated with ADC ($p = 0.015$, $r = +0.63$) and nrCBV ($p = 0.005$, $r = -0.70$).

$\Delta R_{1,ss}$ strongly correlated with K^{trans} in both TN-gliomas ($p = 0.036$, $r = +0.68$) and R-gliomas ($p = 0.0024$, $r = +0.59$; Fig. 3a).

Group differences based on treatment status, IDH status, and Ki67 expression

Differences based on treatment status are shown in Table 3 and Fig. 3b. TN-gliomas had lower $\Delta R_{1,ss}$ (IDH^m/IDH^{wt}: p = 0.026/0.035) and K^{trans} (IDH^m/IDH^{wt}: $p = 0.026/0.17$) than R-gliomas overall, which reflect a lower EEC concentration of CA and a slower CA leakage rate, respectively. In TN-IDH^{wt}, $\Delta R_{2,ss}$* was comparable to R-IDH^{wt} despite the EEC CA being less concentrated, which resulted in significantly higher *TRATE* values ($p = 0.002$; Fig. 3b). *TRATE* > 142 $mM^{-1}s^{-1}$ was exclusively seen in TN-IDH^{wt} (Fig. 3b). TN-IDH^{wt} also had significantly lower PSR ($p = 0.006$), v_e (p = 0.006), and ADC ($p = 0.016$) than R-IDH^{wt}.

Differences based on IDH status are shown in Table 3 and Fig. 3b. TN-IDH^{wt} tended to have more pronounced CA leakage (higher $\Delta R_{1,ss}$ and K^{trans}) than TN-IDH^m (p = 0.13/0.09), as well as higher $\Delta R_{2,ss}$* ($p = 0.09$). Since $\Delta R_{2,ss}$* differences greatly exceeded $\Delta R_{1,ss}$ differences, *TRATE* showed a trend towards being higher in TN-IDH^{wt} than in TN-IDH^m ($p = 0.13$), and TN-IDH^m displayed *TRATE* values comparable to R-gliomas (Table 3; Fig. 3b). In TN, also PSR ($p = 0.13$), v_e ($p = 0.14$), and nrCBV (p = 0.09) tended to differ depending on IDH status. The low sample size in the TN-IDH^m subgroup is probably a reason for such trends not being statistically significant. Notably, nrCBV was the only metric with significantly different values based on IDH status in the recurrent setting.

Differences based on Ki67 expression are shown in Table 4 and Fig. 3c. TN-gliomas with high Ki67 expression had higher *TRATE* ($p = 0.04$), higher nrCBV ($p = 0.001$), and lower PSR values ($p = 0.04$) than low Ki67 lesions

Table 2 Correlations between TRATE and perfusion, permeability, leakage effect, and diffusion MRI metrics

MRI metrics		Treatment-naïve			Recurrent		
		p	r	R^2	p	r	R^2
TRATE	$\Delta R_{1,ss}$	0.32			0.04*	− 0.42	0.18
TRATE	$\Delta R_{2,ss}$*	0.004**	+ 0.71	0.51	0.02*	+ 0.46	0.21
TRATE	PSR	< 0.0001****	− 0.87	0.76	0.0003***	− 0.68	0.46
TRATE	nrCBV	0.02*	+ 0.60	0.36	0.76		
TRATE	K^{trans}	0.77			0.81		
TRATE	v_e	0.31			0.86		
TRATE	ADC	0.04*	− 0.54	0.29	0.12	− 0.33	0.11

p, p-value; r, Pearson's coefficient; R^2, coefficient of determination. r and R^2 are displayed only for correlations that are either significant or trend towards significance. *$p < 0.05$, **$p < 0.01$, ***$p < 0.001$, ****$p < 0.0001$

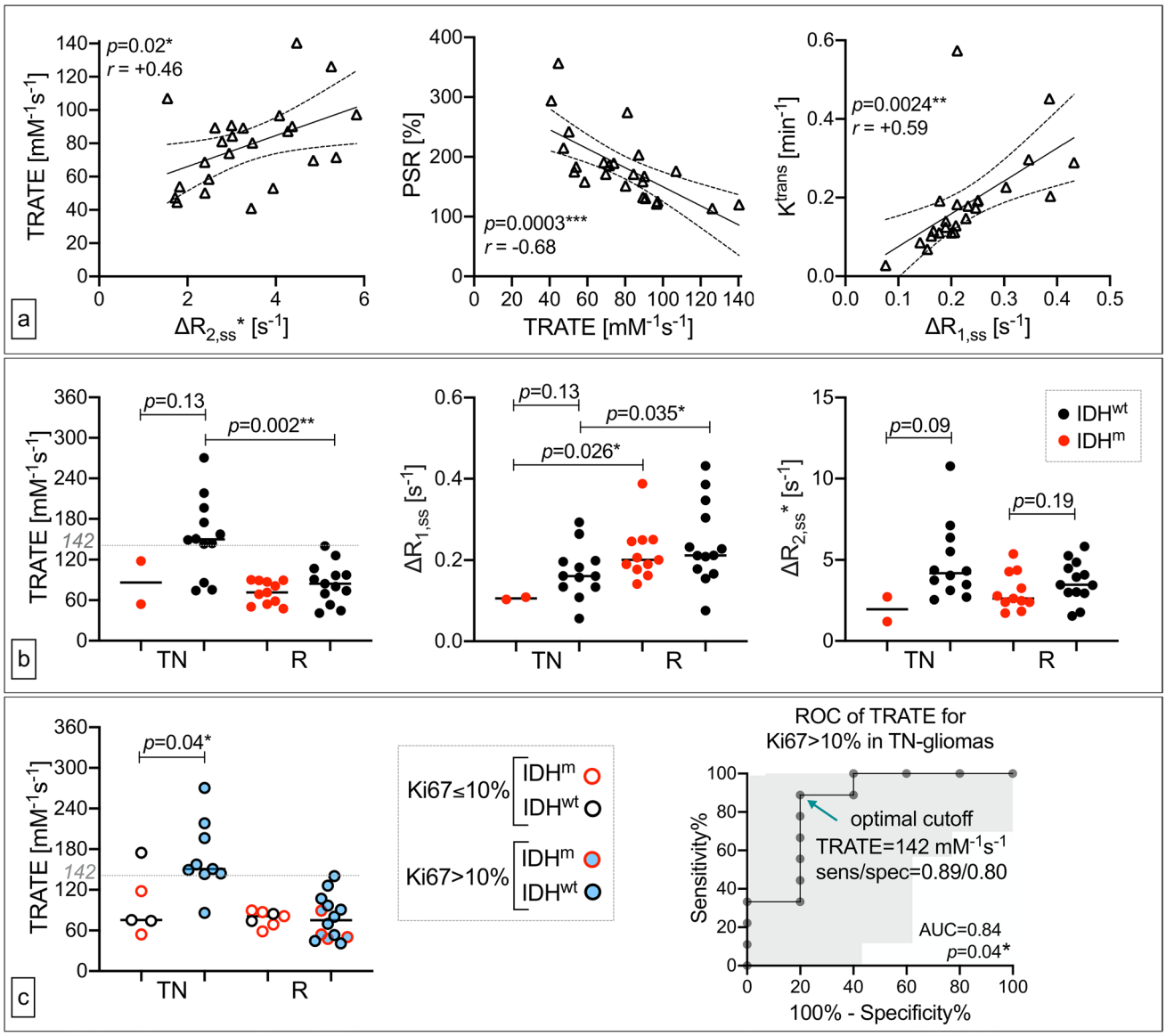

Fig. 3 Correlations among MRI metrics and group differences. Panel **a** shows selected correlations among MRI metrics in R-gliomas, the most numerous subcohort. *TRATE* values depend on $\Delta R_{2,ss}$* and are inversely correlated with PSR values; $\Delta R_{1,ss}$ values are positively correlated with K^{trans}. Panel **b** illustrates group differences in leakage effect metrics according to prior exposure to treatment and IDH status (red vs black). *TRATE* values were higher in TN-IDH^{wt} gliomas compared to their recurrent counterparts, due to comparable $\Delta R_{2,ss}$* values in the presence of lower $\Delta R_{1,ss}$ values. TN-IDH^{wt} gliomas tended to display higher *TRATE* values also compared to IDH^{m} gliomas, ascribable to higher $\Delta R_{2,ss}$* values. Notably, exclusively TN-IDH^{wt} showed median *TRATE* values > 142 mM^{-1}s^{-1}, and only n = 3 TN-IDH^{wt} lesions displayed low *TRATE* (< 142 mM^{-1}s^{-1}). Panel **c** displays *TRATE* differences according to Ki67 expression (white vs blue central color, while the border color reflects IDH status). In TN-gliomas, high Ki67 expression corresponded to higher *TRATE* values. *TRATE* had good diagnostic accuracy (AUC = 0.84) in distinguishing low and high Ki67 gliomas, and a cutoff of > 142 mM^{-1}s^{-1} yielded sensitivity/specificity of 0.89/0.80 for prediction of Ki67 > 10% (see ROC curve with 95% CI). Notably, out of the n = 3 TN-IDH^{wt} lesions with low *TRATE* (**b**), n = 2 had low Ki67 (**c**). TN, treatment-naïve; R, recurrent; IDH^{m}, IDH-mutant; IDH^{wt}, IDH wild-type. *p < 0.05, **p < 0.01, ***p < 0.001, ****p < 0.0001

(Table 4; Fig. 3c). In TN-gliomas, *TRATE* predicted a high Ki67 (> 10%) expression with AUC = 0.84, and a cutoff of *TRATE* > 142 mM^{-1}s^{-1} corresponded to sensitivity and specificity of 89% and 80% (Fig. 3c). Notably, out of n = 3 TN-IDH^{wt} with low *TRATE* (< 142 mM^{-1}s^{-1}), n = 2 had low Ki67 (Fig. 3b, c).

Representative cases

Figure 4 displays perfusion, permeability, and leakage effect MRI maps computed from dynamic SAGE-EPI for representative patients, as well as the disentangled T_1 and T_2* signal contributions, and histopathological images.

Table 3 Differences in MRI metrics based on previous exposure to treatment and IDH status

MRI metrics	Treatment-naïve		Recurrent		*p*-values			
	TN-IDH^{m}	*TN-IDH^{wt}*	*R-IDH^{m}*	*R-IDH^{wt}*	*TN: IDH^{m} vs IDH^{wt}*	*R: IDH^{m} vs IDH^{wt}*	*IDH^{m}: TN vs R*	*IDH^{wt}: TN vs R*
TRATE [mM^{-1}s^{-1}]	86.1 ± 45.1	153.4 ± 58.3	71.6 ± 16.9	85.1 ± 29.6	0.13	0.25	0.64	0.002**
$\Delta R_{1,ss}$ [s^{-1}]	0.11 ± 0.004	0.17 ± 0.06	0.22 ± 0.07	0.24 ± 0.10	0.13	0.57	0.026*	0.035*
$\Delta R_{2,ss}$* [s^{-1}]	2.0 ± 1.0	4.8 ± 2.3	3.0 ± 1.2	3.7 ± 1.3	0.09	0.19	0.41	0.25
PSR [%]	172 ± 65	121 ± 30	192 ± 41	177 ± 72	0.13	0.14	0.78	0.006**
nrCBV	0.72 ± 0.58	2.15 ± 0.74	1.20 ± 0.36	2.17 ± 0.97	0.09	0.02*	0.15	0.93
K^{trans} [min^{-1}]	0.06 ± 0.006	0.16 ± 0.12	0.14 ± 0.04	0.22 ± 0.15	0.09	0.11	0.026*	0.17
v_e	0.48 ± 0.07	0.28 ± 0.14	0.34 ± 0.14	0.49 ± 0.18	0.14	0.055	0.23	0.006**
ADC [× 10^{-6} mm^2/s]	1118 ± 107	977 ± 240	1227 ± 155	1228 ± 199	0.35	0.95	0.51	0.016*

Group values for MRI metrics are reported as mean ± standard deviation. *$p < 0.05$, **$p < 0.01$, ***$p < 0.001$, ****$p < 0.0001$. *TN*, treatment-naïve; *R*, recurrent; *IDH^{m}*, IDH-mutant; *IDH^{wt}*, IDH wild-type

Table 4 Differences in MRI metrics based on Ki67 expression

MRI metrics	Treatment-naïve			Recurrent		
	Ki67 ≤ 10%	*Ki67 > 10%*	*p*	*Ki67 ≤ 10%*	*Ki67 > 10%*	*p*
TRATE [mM^{-1}s^{-1}]	99.3 ± 48.2	168.5 ± 53.0	0.04*	77.6 ± 11.2	77.9 ± 31.8	0.86
$\Delta R_{1,ss}$ [s^{-1}]	0.19 ± 0.09	0.14 ± 0.04	0.36	0.19 ± 0.04	0.23 ± 0.10	0.44
$\Delta R_{2,ss}$* [s^{-1}]	3.8 ± 2.2	4.8 ± 2.6	0.60	2.9 ± 0.6	3.2 ± 1.2	0.58
PSR [%]	159 ± 47	111 ± 16	0.04*	189 ± 45	186 ± 70	0.53
nrCBV	1.02 ± 0.45	2.46 ± 0.55	0.001**	1.23 ± 0.73	1.81 ± 0.97	0.11
K^{trans} [min^{-1}]	0.20 ± 0.17	0.12 ± 0.05	0.70	0.13 ± 0.04	0.21 ± 0.15	0.25
v_e	0.37 ± 0.12	0.28 ± 0.16	0.24	0.37 ± 0.15	0.45 ± 0.19	0.36
ADC [× 10^{-6} mm^2/s]	1107 ± 256	936 ± 200	0.19	1293 ± 183	1202 ± 176	0.44

Group values for MRI metrics are reported as mean ± standard deviation, p = p-value. *$p < 0.05$, **$p < 0.01$, ***$p < 0.001$, ****$p < 0.0001$. *TN*, treatment-naïve; *R*, recurrent; *IDH^{m}*, IDH-mutant; *IDH^{wt}*, IDH wild-type

Discussion

This study demonstrates the feasibility of computing perfusion (DSC), permeability (DCE), and quantitative maps derived from contrast leakage effects from a *single* dynamic SAGE-EPI sequence with a *single bolus* of contrast agent. Additionally, this study demonstrated that such leakage effect metrics (i.e., $\Delta R_{1,ss}$, $\Delta R_{2,ss}$*, *TRATE*) in gliomas depend on previous exposure to treatment, IDH status, and Ki67 expression. While simultaneous DSC and DCE were already proposed in human patients by Stokes et al [31] and *TRATE* computation was originally proposed mainly in the preclinical setting by Semmineh et al [33], this is the first study proposing a pipeline to *simultaneously* compute DSC, DCE, and leakage effect maps in human gliomas, and assessing their biological correlates.

This approach has multiple clinical benefits. First, dynamic SAGE-EPI is 3 minutes long (extending to 5–6 min may be considered—see the limitations section), while separate DSC and DCE would require at least 10 min of total scanning time. This is clinically relevant because brain tumor patients already undergo very time-consuming protocols, including multiple advanced and functional sequences [17, 48], which are a burden for patients. Second, simultaneous acquisition eliminates the need of a second bolus of contrast agent (CA). Double-dose CA raises concerns for chronic gadolinium deposition in deep gray matter [29] and for adverse effects in patients with impaired renal function [30], especially considering that brain tumor patients undergo serial follow-up MRI with CA. Dynamic SAGE-EPI would allow to perform DSC and DCE at every timepoint with a remarkable cumulative reduction of administered CA. Third, our pipeline allows the quantification of leakage effects, which provide further complementary insights into vascular permeability and tissue cytoarchitecture, as further discussed.

In the present study, $\Delta R_{1,ss}$, which is thought to be proportional to CA concentration in the extravascular

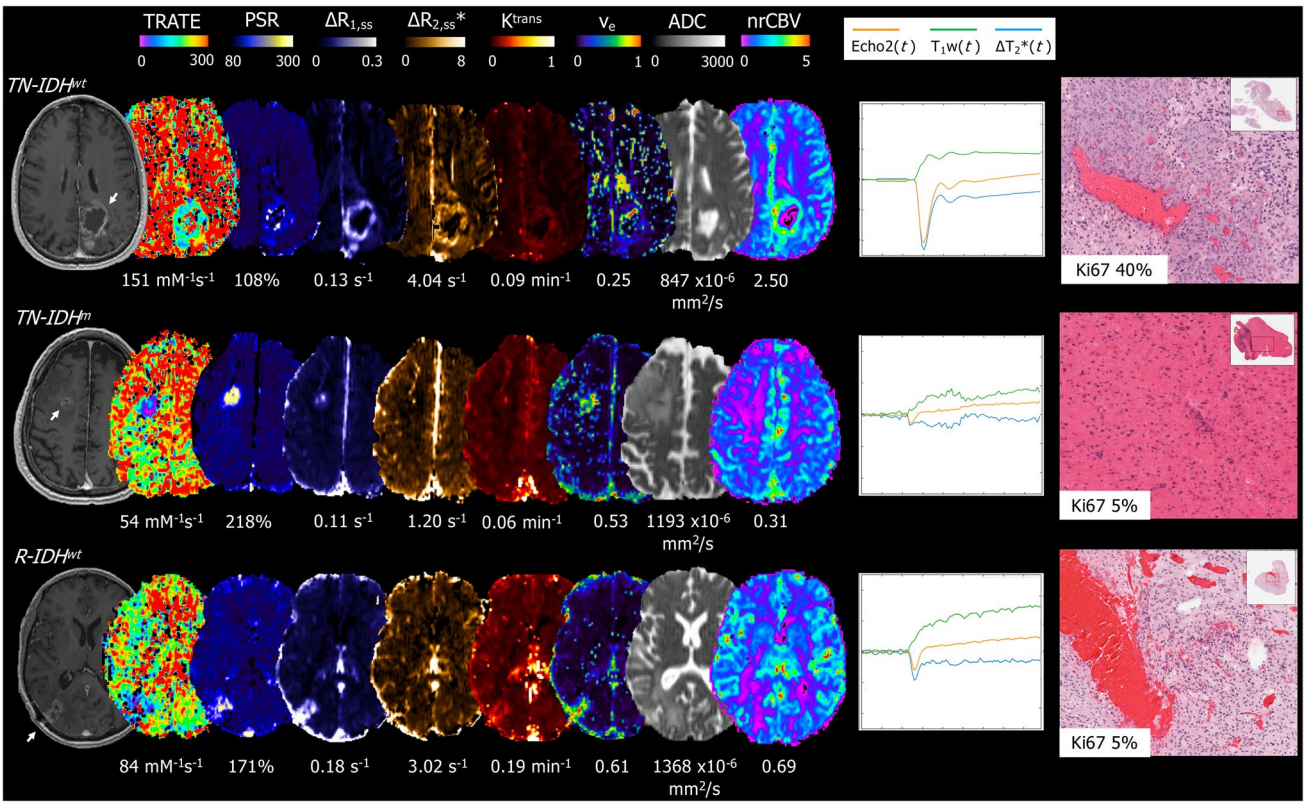

Fig. 4 Representative cases. Perfusion, permeability, and leakage effect maps derived from dynamic SAGE-EPI in three enhancing gliomas (TN-IDH^{wt}, TN-IDH^{m}, and R-IDH^{wt}, respectively) are displayed along with the disentangled T_1 (green line) and T_2* (blue line) signal contributions, with histopathological H&E slides, and with their appearance on post-contrast T_1-weighted images (arrows). The TN-IDH^{wt} glioma (top row) displays higher *TRATE* values, driven by more pronounced T_2*-leakage effects ($\Delta R_{2,ss}$* map and blue line) compared to T1-leakage effects ($\Delta R_{1,ss}$ map and green line). Histopathology showed high cellularity, microvascular proliferation, and high Ki67 expression. The TN-IDH^{m} glioma (middle row) displays lower *TRATE* values, as well as lower cell density and Ki67. The R-IDH^{wt} glioma (bottom row) shows lower *TRATE* due to similar T_2*-leakage effects ($\Delta R_{2,ss}$* map and blue line) in the presence of more prominent T_1-leakage effects ($\Delta R_{1,ss}$ map and green line). Histopathology showed recurrent tumor mixed with treatment effects, including reactive gliosis, hyalinized vessels, and foci of necrosis. TN, treatment-naïve; R, recurrent; IDH^{m}, IDH-mutant; IDH^{wt}, IDH wild-type

extracellular compartment (EEC) [32, 33], was found to correlate with K^{trans}, representing the rate of CA leakage from the intravascular (IV) compartment to EEC [10, 12]. The exposure to previous treatment was associated both with higher $\Delta R_{1,ss}$ and K^{trans}, reflecting a more prominent and faster CA leakage in EEC. This is consistent with the well-established notion that radiation increases blood–brain barrier (BBB) permeability [49–51]. These two findings advocate for $\Delta R_{1,ss}$ as a quantitative biomarker of BBB breakdown, and suggest that it could be a surrogate of K^{trans}. This is relevant because K^{trans} values are dramatically affected by the AIF selection and the pharmacokinetic model fit [52], which leads to highly variable measurements. For instance, average K^{trans} values [min^{-1}] in glioblastoma cohorts ranged 0.035–1.8 across studies [21, 31, 53–55] (0.16 in this study). Conversely, $\Delta R_{1,ss}$ [s^{-1}] is a simpler metric, independent from model fit or AIF. Therefore, $\Delta R_{1,ss}$, if further validated, would constitute a more universal quantitative biomarker for blood–brain barrier (BBB) breakdown.

TRATE showed characteristic high values in treatment-naïve (TN) IDH^{wt}, which were the only tumors displaying *TRATE* > 142 $mM^{-1}s^{-1}$. Additionally, *TRATE* > 142 $mM^{-1}s^{-1}$ in TN-gliomas predicted high Ki67 expression with good diagnostic performance (sensitivity/specificity: 0.89/0.80), and the few TN-IDH^{wt} with low *TRATE* values almost entirely had low Ki67 expression. Preclinical and simulated data by Semmineh et al [33] suggest that *TRATE* may be a cytoarchitectural biomarker, displaying higher values in the presence of higher cell volume fraction and/or larger cell size. Our results, taken together, are consistent with this interpretation. Higher *TRATE* values in IDH^{wt} gliomas (i.e., glioblastomas, as per 2021 WHO classification [1]) are consistent with their established higher cell density and proliferation rate, compared to lower grades [56]. As for Ki67 expression, while it does not directly represent cell

density nor cell size, it is a biomarker of active cell proliferation [46, 47], and it is reasonable to speculate that gliomas with higher proliferation rate may also have higher cellularity as a result. Finally, lower *TRATE* values in gliomas exposed to treatment can be explained with the notion that the enhancing regions in recurrent (R) gliomas are possibly characterized by a lower cellularity overall, due to a combination of malignant cells and treatment effects, including hyaline vasculopathy, reactive gliosis, and radiation necrosis, which were documented in histopathological reports in 50% of R-gliomas in our cohort. This explanation is also supported by higher values of other metrics reflecting the amplitude of EEC (i.e., ADC and v_e) in our recurrent subcohort. Further studies longitudinally comparing *TRATE* and $\Delta R_{1,ss}$ values before and after chemoradiation are warranted to better understand the treatment-induced changes in these novel metrics, along with their potential role for treatment response assessment.

PSR values displayed similar group differences compared to TRATE, but with opposite direction, and these two metrics had a strong inverse correlation. Although PSR is easier to obtain, *TRATE* should be considered a *refined* measure of the balance between T_2*- and T_1-leakage effects compared to PSR, as it is measured in units and insensitive to acquisition parameters (i.e., FA and TE). Additionally, the pipeline for *TRATE* computation has the advantage of *separately* quantifying T_2*- and T_1-leakage effects (by computing $\Delta R_{2,ss}$* and $\Delta R_{1,ss}$, respectively), therefore providing additional information. Nevertheless, our results suggest that institutions where *TRATE* computation is not yet available may use PSR to obtain cytoarchitectural insights, with the *caveat* of its dependency upon TE and FA.

A potential objection to the usefulness of *TRATE* is that ADC is a well-established proxy of cell density in gliomas [17, 57], and it is easier to obtain in the clinical setting. However, ADC values are thought to mainly reflect the amplitude of EEC, and also to be influenced by the extracellular matrix composition [58, 59]. Conversely, *TRATE* values are thought to depend on the steepness of the susceptibility gradients induced by CA molecules in EEC onto the extravascular intracellular compartment (EIC), which depends on the clustering of CA molecules in EEC and their proximity to cell membranes. Therefore, leakage effect measurements, as assessed by *TRATE* or PSR, provide a unique cytoarchitectural contrast that ultimately depends on the combination of cell volume fraction and cell size. This interpretation, depicted in Fig. 5 and elaborated in light of previous studies [32, 33], is also supported by our observation that the correlation between *TRATE* and ADC was only moderate in the TN-gliomas and non-significant in R-gliomas, and by Semmineh et al [33] reporting a low voxel-wise correlation between *TRATE* and ADC. Additionally, previous literature showed that PSR values performed better than ADC in some applications such as differential diagnosis [60], probably due to the unique contrast of leakage effect measurements, reflecting cytoarchitecture. To note, other studies

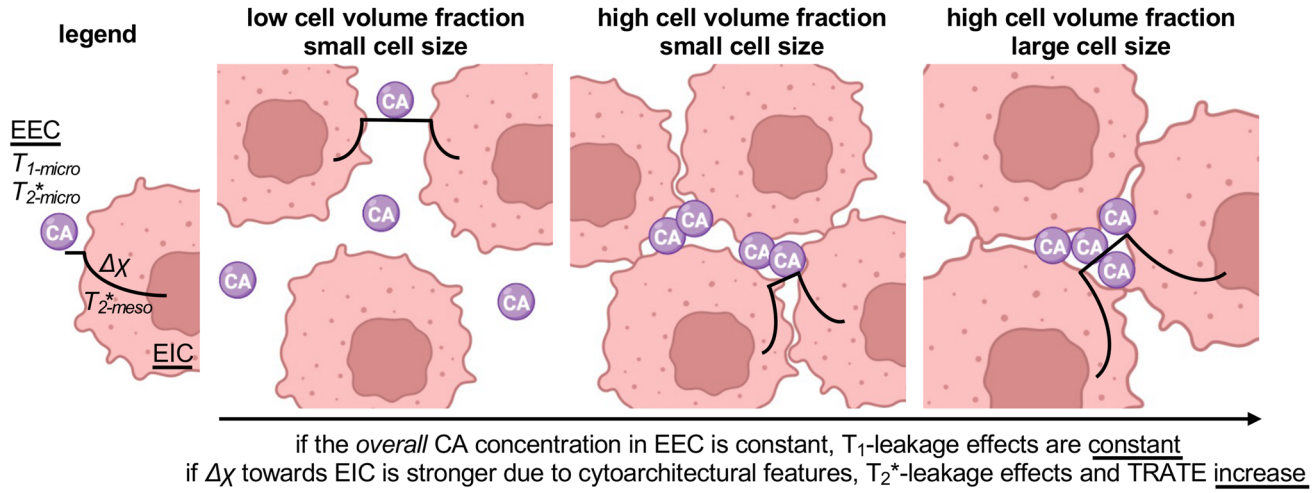

Fig. 5 Schematic interpretation of contrast agent (CA) leakage effects in T_2*-weighted DSC perfusion imaging. After leaking, CA induces T_1 and T_2* *microscopic* leakage effects in the extravascular extracellular compartment (EEC), as well as T_2* *mesoscopic* leakage effects that take place also in the extravascular intracellular compartment (EIC) due to susceptibility gradients ($\Delta\chi$) arising in the CA proximity. While microscopic effects only depend on CA concentration, mesoscopic effects are thought to be enhanced by a higher cell volume fraction and/or a larger cell size, possibly due to an increased CA packing in the proximity of cell membranes, which results in a stronger $\Delta\chi$ (the black lines represent the steepness of $\Delta\chi$, which progressively increases from the left panel to the right panel, consistently with CA clustering). Conversely, ADC is sensitive to EEC amplitude but not to cytoarchitecture; therefore, ADC values in the right panel may be comparable to the central panel

Table 5 Hypothesized pathophysiologic interpretation of dynamic SAGE-EPI metrics in gliomas

Biologic correlates	Underlying pathophysiologic event	MRI metrics
↑ Vascular density	Angiogenesis	↑ nrCBV
↑ Vascular permeability	BBB disruption linked to angiogenesis and/or treatment-induced effects	↑ K^{trans}, ↑ $\Delta R_{1,ss}$
↑ Cell volume fraction *	Tumor proliferation	↑ TRATE, ↓ PSR, ↓ v_e
↓ Cell size *	Tumor cell shrinkage following cytotoxic treatment	↓ TRATE, ↑ PSR

*TRATE and PSR differences due to cell volume fraction and cell size differences may also be exploited for differential diagnosis. Note that the proposed interpretations are partly based on speculation, and not all these correlates have been demonstrated. *BBB*, blood–brain barrier

have proposed to predict cell density with relaxometry [61] and deep learning methods [62], and to assess cell size with diffusion biophysical models [63]. As an overview, Table 5. reports a hypothesized pathophysiologic interpretation of dynamic SAGE-EPI metrics.

This study has some limitations, including being a single-institution study. Future studies may compare *TRATE* values across institutions, to validate it as a parameter-insensitive leakage effect measurement compared to PSR, while being aware that *TRATE* values still depend on CA type and field strength. An immediate benchmark for this comparison would be the differential diagnosis, a well-established PSR application. Another limitation of this article is the lack of histopathological quantitative validation assessing *TRATE* association with cell volume fraction and cell size. Moreover, we did not perform a separate set of experiments to validate and compare DCE obtained from our pipeline with traditional DCE, because this would have required separate injections of contrast, with a study design similar to other articles evaluating DSC metrics with and without preload [31, 36]. The proposed DCE analysis differs from a traditional DCE because it is performed on T_1w signal extrapolated from EPI acquisitions, and it has lower spatial resolution and a shorter acquisition time (~ 3 min vs ~ 5–6 min in typical DCE sequences optimized for brain tumors) [14, 64, 65]. EPI acquisitions result in more pronounced susceptibility artifacts in the proximity of tissue-air interfaces, constituting a limitation only for lesions located in temporal poles and fronto-basal gyri. A lower spatial resolution limits the assessment of subtle tumor heterogeneity, but does not impact our estimation of median K^{trans} and v_e within tumor tissue. The shorter acquisition time may affect the accuracy of DCE metrics and leakage effect metrics, since CA leakage is thought to reach an equilibrium in 5–10 min [33]. Future studies may explore dynamic SAGE-EPI with a longer acquisition time to solve this potential limitation. Future studies may also explore the potential validity of our methodology in non-enhancing gliomas, for which the utility of metrics related to CA extravasation (K^{trans}, v_e, $\Delta R_{1,ss}$, *TRATE*) is more ambiguous, since no gross CA extravasation is seen on T_1w anatomical images. Additionally, it is worth mentioning that, while the proposed pipeline is feasible with a simpler dual-echo GE DSC, dynamic SAGE-EPI also contains additional echoes that can be used to perform additional vessel size imaging (VSI) [11] and vessel architecture imaging (VAI) [66]. Finally, this study was aimed at proposing a simultaneous analysis for multiple imaging metrics, rather than assessing nrCBV accuracy. Our proposed methodology *as it is* is not compliant with the current DSC guidelines, which advise for single-echo DSC using either 60° FA with preload or 30° FA without preload [67]. However, we employed a bidirectional leakage correction algorithm that minimizes the impact of pulse sequence parameters on nrCBV calculation [43]. If compliance with guidelines is desired, an easy solution would be to change dynamic SAGE-EPI FA to 30°, in order to obtain simultaneous guideline-compliant DSC, DCE, and leakage effect metrics with only one dose of contrast. This should not impact leakage effect measurements, since dual-echo computed signals (e.g., $\Delta R_2^*(t)$) should be minimally impacted by pulse sequence parameters [31]. However, in our protocol, FA is set to 90° because lowering the FA would result in very low signal from the spin echo sequences included in dynamic SAGE-EPI, which would affect VSI and VAI. An alternative possible solution would be to compute nrCBV from dual-echo derived $\Delta R_2^*(t)$, an approach that has been shown to be as accurate as single-echo DSC with preload [31], and which may be eventually incorporated in future guidelines.

Conclusions

We propose an image processing pipeline to generate perfusion, permeability, and novel leakage effect quantitative maps from a *single* dynamic SAGE-EPI sequence with a single bolus of contrast agent. This method can reduce scanning time and halve contrast agent administration compared to acquiring two separate sequences for perfusion and permeability imaging, and provides complementary leakage effect metrics. Among leakage effect metrics, $\Delta R_{1,ss}$ shows potential as a quantitative biomarker for blood–brain barrier breakdown, while *TRATE* represents a refined version of

PSR, which may capture unique cytoarchitectural information dependent on cell volume fraction and cell size.

Supplementary Information The online version contains supplementary material available at https://doi.org/10.1007/s00330-023-10215-z.

Acknowledgements The authors are thankful to (in alphabetical order) Nicoletta Anzalone, Stefano Bastianello, Antonella Castellano, Eduardo Caverzasi, Gian Marco Conte, Andrea Falini, Anna Pichiecchio, and Valentina Pieri for the valuable discussion about the results of this study.

Funding This project was funded by the training grants NIH NIGMS T32 GM008042 (NSC), NIH NCI R01CA270027 (BME), NIH NCI R01CA279984 (BME), NIH NCI P50CA211015 (LML), and DoD CA20029 (BME).

Declarations

Guarantor The scientific guarantor of this publication is Benjamin M Ellingson, University of California Los Angeles.

Conflict of interest Disclosures relevant to the topic of the manuscript: BME owns the patent for dynamic SAGE-EPI (patent: US 11,378,638 B2).
The authors of this manuscript declare relationships with the following companies (not relevant to the topic of the manuscript):
JO is currently employed by Rampart Bioscience. TFC is a cofounder, major stock holder, consultant, and board member of Katmai Pharmaceuticals, is a member of the board for the 501c3 Global Coalition for Adaptive Research, holds stock option of Notable Labs, holds stock in Chimerix, receives milestone payments and possible future royalties, is a member of the scientific advisory board for Break Through Cancer, is a member of the scientific advisory board for Cure Brain Cancer Foundation, has provided paid consulting services to GCAR; Gan & Lee; BrainStorm; Katmai; Sapience; Inovio; Vigeo Therapeutics; DNATrix; Tyme; SDP; Novartis; Roche; Kintara; Bayer; Merck; Boehinger Ingelheim; VBL; Amgen; Kiyatec; Odonate Therapeutics QED; Medefield; Pascal Biosciences; Tocagen; Karyopharm; GW Pharma; Abbvie; VBI; Deciphera; Agios; Genocea; Celgene; Puma; Lilly; BMS; Cortice; Wellcome Trust; Novocure; Novogen; Boston Biomedical; Sunovion; Human Longevity; Insys; ProNai; Pfizer; Notable labs; Medqia Trizel; Medscape, and has contracts with UCLA for the Brain Tumor Program with Oncovir; Merck; Oncoceutics; Novartis; Amgen; Abbvie; DNAtrix; Beigene; BMS; AstraZeneca; Kazia; Agios; Boston Biomedical; Deciphera; Tocagen; Orbus; and Karyopharm. BME is a paid advisor and consultant for Medicenna, MedQIA, Neosoma, Servier Pharmaceuticals, Siemens, Janssen, Imaging Endpoints, Kazia, VBL, Oncoceutics/Chimerix, Sumitomo Dainippon Pharma Oncology, ImmunoGenesis, Ellipses Pharma, Monteris, Global Coalition for Adaptive Research (GCAR), Alpheus Medical, Inc., Curtana Pharma, and Sagimet Biosciences. Grant funding is from Siemens, Servier/Agios, Neosoma, and Janssen.

Statistics and biometry No complex statistical methods were necessary for this paper.

Informed consent Written informed consent was obtained from all subjects (patients) in this study.

Ethical approval Institutional Review Board approval was obtained (IRB#14-001261 and #21-000514) from the local ethic committee (University of California Los Angeles).

Study subjects or cohorts overlap Some study subjects or cohorts have been previously reported in:

Chakhoyan et al 2018, Validation of vessel size imaging (VSI) in high-grade human gliomas using magnetic resonance imaging, image-guided biopsies, and quantitative immunohistochemistry.

Methodology
- prospective
- diagnostic or prognostic study
- performed at one institution

References

1. Louis DN, Perry A, Wesseling P et al (2021) The 2021 WHO Classification of Tumors of the Central Nervous System: a summary. Neuro Oncol 23:1231–1251. https://doi.org/10.1093/neuonc/noab106
2. Tabouret E, Nguyen AT, Dehais C et al (2016) Prognostic impact of the 2016 WHO classification of diffuse gliomas in the French POLA cohort. Acta Neuropathol 132:625–634. https://doi.org/10.1007/s00401-016-1611-8
3. Carabenciov ID, Buckner JC (2019) Controversies in the therapy of low-grade gliomas. Curr Treat Options Oncol 20:25. https://doi.org/10.1007/s11864-019-0625-6
4. Cloughesy TF, Mochizuki AY, Orpilla JR et al (2019) Neoadjuvant anti-PD-1 immunotherapy promotes a survival benefit with intratumoral and systemic immune responses in recurrent glioblastoma. Nat Med 25:477–486. https://doi.org/10.1038/s41591-018-0337-7
5. Ellingson BM, Kim HJ, Woodworth DC et al (2014) Recurrent glioblastoma treated with bevacizumab: contrast-enhanced T1-weighted subtraction maps improve tumor delineation and aid prediction of survival in a multicenter clinical trial. Radiology 271:200–210. https://doi.org/10.1148/radiol.13131305
6. Hanahan D, Weinberg RA (2000) The hallmarks of cancer. Cell 100:57–70. https://doi.org/10.1016/s0092-8674(00)81683-9
7. Domènech M, Hernández A, Plaja A, et al (2021) Hypoxia: the cornerstone of glioblastoma. Int J Mol Sci 22: https://doi.org/10.3390/ijms222212608
8. Kane JR (2019) The role of brain vasculature in glioblastoma. Mol Neurobiol 56:6645–6653. https://doi.org/10.1007/s12035-019-1561-y
9. Das S, Marsden PA (2013) Angiogenesis in glioblastoma. N Engl J Med 369:1561–1563. https://doi.org/10.1056/NEJMcibr1309402
10. Zhang J, Liu H, Tong H, et al (2017) Clinical applications of contrast-enhanced perfusion MRI techniques in gliomas: recent advances and current challenges. Contrast Media Mol Imaging 2017: https://doi.org/10.1155/2017/7064120
11. Chakhoyan A, Yao J, Leu K et al (2019) Validation of vessel size imaging (VSI) in high-grade human gliomas using magnetic

resonance imaging, image-guided biopsies, and quantitative immunohistochemistry. Sci Rep 9:2846. https://doi.org/10.1038/s41598-018-37564-w
12. Tofts PS, Brix G, Buckley DL et al (1999) Estimating kinetic parameters from dynamic contrast-enhanced T(1)-weighted MRI of a diffusable tracer: standardized quantities and symbols. J Magn Reson Imaging 10:223–232. https://doi.org/10.1002/(sici)1522-2586(199909)10:3%3c223::aid-jmri2%3e3.0.co;2-s
13. Brendle C, Hempel JM, Schittenhelm J et al (2018) Glioma grading and determination of IDH mutation status and ATRX loss by DCE and ASL perfusion. Clin Neuroradiol 28:421–428. https://doi.org/10.1007/s00062-017-0590-z
14. Anzalone N, Castellano A, Cadioli M et al (2018) Brain gliomas: multicenter standardized assessment of dynamic contrast-enhanced and dynamic susceptibility contrast MR images. Radiology 287:933–943. https://doi.org/10.1148/radiol.2017170362
15. Delgado AF, Delgado AF (2017) Discrimination between glioma grades II and III using dynamic susceptibility perfusion MRI: a meta-analysis. AJNR Am J Neuroradiol 38:1348–1355. https://doi.org/10.3174/ajnr.A5218
16. Zhang HW, lyu GW, He WJ, et al (2020) DSC and DCE histogram analyses of glioma biomarkers, including IDH, MGMT, and TERT, on differentiation and survival. Acad Radiol 1–9. https://doi.org/10.1016/j.acra.2019.12.010
17. Sanvito F, Castellano A, Falini A (2021) Advancements in neuroimaging to unravel biological and molecular features of brain tumors. Cancers (Basel) 13:1–25. https://doi.org/10.3390/cancers13030424
18. Leu K, Ott GA, Lai A et al (2017) Perfusion and diffusion MRI signatures in histologic and genetic subtypes of WHO grade II–III diffuse gliomas. J Neurooncol 134:177–188. https://doi.org/10.1007/s11060-017-2506-9
19. Kickingereder P, Sahm F, Radbruch A et al (2015) IDH mutation status is associated with a distinct hypoxia/angiogenesis transcriptome signature which is non-invasively predictable with rCBV imaging in human glioma. Sci Rep 5:1–9. https://doi.org/10.1038/srep16238
20. Zhao J, Yang Z, Luo B et al (2015) Quantitative evaluation of diffusion and dynamic contrast-enhanced MR in tumor parenchyma and peritumoral area for distinction of brain tumors. PLoS One 10:e0138573. https://doi.org/10.1371/journal.pone.0138573
21. Kickingereder P, Sahm F, Wiestler B et al (2014) Evaluation of microvascular permeability with dynamic contrast-enhanced MRI for the differentiation of primary CNS lymphoma and glioblastoma: radiologic-pathologic correlation. AJNR Am J Neuroradiol 35:1503–1508. https://doi.org/10.3174/ajnr.A3915
22. Chaganti J, Taylor M, Woodford H, Steel T (2021) Differentiation of primary central nervous system lymphoma and high-grade glioma with dynamic susceptibility contrast-derived metrics: pilot study. World Neurosurg 151:e979–e987. https://doi.org/10.1016/j.wneu.2021.05.026
23. Pons-Escoda A, Garcia-Ruiz A, Naval-Baudin P et al (2020) Presurgical identification of primary central nervous system lymphoma with normalized time-intensity curve: a pilot study of a new method to analyze DSC-PWI. AJNR Am J Neuroradiol 41:1816–1824. https://doi.org/10.3174/ajnr.A6761
24. Pons-Escoda A, Smits M (2023) Dynamic-susceptibility-contrast perfusion-weighted-imaging (DSC-PWI) in brain tumors: a brief up-to-date overview for clinical neuroradiologists. Eur Radiol https://doi.org/10.1007/s00330-023-09729-3
25. Strauss SB, Meng A, Ebani EJ, Chiang GC (2019) Imaging glioblastoma posttreatment: progression, pseudoprogression, pseudoresponse, radiation necrosis. Radiol Clin North Am. 57:1199–1216
26. Muto M, Frauenfelder G, Senese R et al (2018) Dynamic susceptibility contrast (DSC) perfusion MRI in differential diagnosis between radionecrosis and neoangiogenesis in cerebral metastases using rCBV, rCBF and K2. Radiol Med 123:545–552. https://doi.org/10.1007/s11547-018-0866-7
27. Shin KE, Ahn KJ, Choi HS et al (2014) DCE and DSC MR perfusion imaging in the differentiation of recurrent tumour from treatment-related changes in patients with glioma. Clin Radiol 69:e264-72. https://doi.org/10.1016/j.crad.2014.01.016
28. Manfrini E, Smits M, Thust S et al (2021) From research to clinical practice: a European neuroradiological survey on quantitative advanced MRI implementation. Eur Radiol 31:6334–6341. https://doi.org/10.1007/s00330-020-07582-2
29. Gulani V, Calamante F, Shellock FG et al (2017) Gadolinium deposition in the brain: summary of evidence and recommendations. Lancet Neurol 16:564–570. https://doi.org/10.1016/S1474-4422(17)30158-8
30. Weinreb JC, Rodby RA, Yee J et al (2021) Use of intravenous gadolinium-based contrast media in patients with kidney disease: consensus statements from the American College of Radiology and the National Kidney Foundation. Radiology 298:28–35. https://doi.org/10.1148/radiol.2020202903
31. Stokes AM, Bergamino M, Alhilali L et al (2021) Evaluation of single bolus, dual-echo dynamic susceptibility contrast MRI protocols in brain tumor patients. J Cereb Blood Flow Metab 41:3378–3390. https://doi.org/10.1177/0271678X211039597
32. Quarles CC, Gochberg DF, Gore JC, Yankeelov TE (2009) A theoretical framework to model DSC-MRI data acquired in the presence of contrast agent extravasation. Phys Med Biol 54:5749–5766. https://doi.org/10.1088/0031-9155/54/19/006
33. Semmineh NB, Xu J, Skinner JT et al (2015) Assessing tumor cytoarchitecture using multiecho DSC-MRI derived measures of the transverse relaxivity at tracer equilibrium (TRATE). Magn Reson Med 74:772–784. https://doi.org/10.1002/mrm.25435
34. Mangla R, Kolar B, Zhu T et al (2011) Percentage signal recovery derived from MR dynamic susceptibility contrast imaging is useful to differentiate common enhancing malignant lesions of the brain. AJNR Am J Neuroradiol 32:1004–1010. https://doi.org/10.3174/ajnr.A2441
35. Lee MD, Baird GL, Bell LC et al (2019) Utility of percentage signal recovery and baseline signal in DSC-MRI optimized for relative CBV measurement for differentiating glioblastoma, lymphoma, metastasis, and meningioma. AJNR Am J Neuroradiol 40:1445–1450. https://doi.org/10.3174/ajnr.A6153
36. Boxerman JL, Paulson ES, Prah MA, Schmainda KM (2013) The effect of pulse sequence parameters and contrast agent dose on percentage signal recovery in DSC-MRI: implications for clinical applications. AJNR Am J Neuroradiol 34:1364–1369. https://doi.org/10.3174/ajnr.A3477
37. Ellingson BM, Bendszus M, Boxerman J et al (2015) Consensus recommendations for a standardized Brain Tumor Imaging Protocol in clinical trials. Neuro Oncol 17:1188–1198. https://doi.org/10.1093/neuonc/nov095
38. Schmiedeskamp H, Straka M, Newbould RD et al (2012) Combined spin- and gradient-echo perfusion-weighted imaging. Magn Reson Med 68:30–40. https://doi.org/10.1002/mrm.23195
39. Schmiedeskamp H, Straka M, Bammer R (2012) Compensation of slice profile mismatch in combined spin- and gradient-echo echo-planar imaging pulse sequences. Magn Reson Med 67:378–388. https://doi.org/10.1002/mrm.23012
40. Welker K, Boxerman J, Kalnin A et al (2015) ASFNR recommendations for clinical performance of MR dynamic susceptibility contrast perfusion imaging of the brain. AJNR Am J Neuroradiol 36:E41–E51. https://doi.org/10.3174/ajnr.A4341
41. Conte GM, Altabella L, Castellano A et al (2019) Comparison of T1 mapping and fixed T1 method for dynamic contrast-enhanced MRI perfusion in brain gliomas. Eur Radiol 29:3467–3479. https://doi.org/10.1007/s00330-019-06122-x

42. Rohrer M, Bauer H, Mintorovitch J et al (2005) Comparison of magnetic properties of MRI contrast media solutions at different magnetic field strengths. Invest Radiol 40:715–724. https://doi.org/10.1097/01.rli.0000184756.66360.d3
43. Leu K, Boxerman JL, Cloughesy TF et al (2016) Improved leakage correction for single-echo dynamic susceptibility contrast perfusion MRI estimates of relative cerebral blood volume in high-grade gliomas by accounting for bidirectional contrast agent exchange. AJNR Am J Neuroradiol 37:1440–1446. https://doi.org/10.3174/ajnr.A4759
44. Evans JD (1996) Straightforward statistics for the behavioral sciences. Thomson Brooks/Cole Publishing Co
45. Sanvito F, Palesi F, Rognone E et al (2022) Impact of the inversion time on regional brain perfusion estimation with clinical arterial spin labeling protocols. MAGMA 35:349–363. https://doi.org/10.1007/s10334-021-00964-7
46. Zhang Z, Gu W, Hu M et al (2022) Based on clinical Ki-67 expression and serum infiltrating lymphocytes related nomogram for predicting the diagnosis of glioma-grading. Front Oncol 12:696037. https://doi.org/10.3389/fonc.2022.696037
47. Skjulsvik AJ, Mørk JN, Torp MO, Torp SH (2014) Ki-67/MIB-1 immunostaining in a cohort of human gliomas. Int J Clin Exp Pathol 7:8905–8910
48. Castellano A, Falini A (2016) Progress in neuro-imaging of brain tumors. Curr Opin Oncol 28:484–493. https://doi.org/10.1097/CCO.0000000000000328
49. Blethen KE, Sprowls SA, Arsiwala TA et al (2023) Effects of whole-brain radiation therapy on the blood-brain barrier in immunocompetent and immunocompromised mouse models. Radiat Oncol 18:22. https://doi.org/10.1186/s13014-023-02215-6
50. Wilson CM, Gaber MW, Sabek OM et al (2009) Radiation-induced astrogliosis and blood-brain barrier damage can be abrogated using anti-TNF treatment. Int J Radiat Oncol Biol Phys 74:934–941. https://doi.org/10.1016/j.ijrobp.2009.02.035
51. van Vulpen M, Kal HB, Taphoorn MJB, El-Sharouni SY (2002) Changes in blood-brain barrier permeability induced by radiotherapy: implications for timing of chemotherapy? (Review). Oncol Rep 9:683–688
52. Woodall RT, Sahoo P, Cui Y, et al (2021) Repeatability of tumor perfusion kinetics from dynamic contrast-enhanced MRI in glioblastoma. Neurooncol Adv 3:vdab174. https://doi.org/10.1093/noajnl/vdab174
53. Cetinkaya E, Aralasmak A, Atasoy B et al (2022) Dynamic contrast-enhanced MR perfusion in differentiation of benign and malignant brain lesions. Curr Med imaging 18:1099–1105. https://doi.org/10.2174/1573405618666220324112457
54. Ahn SS, Shin NY, Chang JH et al (2014) Prediction of methylguanine methyltransferase promoter methylation in glioblastoma using dynamic contrast-enhanced magnetic resonance and diffusion tensor imaging: clinical article. J Neurosurg 121:367–373. https://doi.org/10.3171/2014.5.JNS132279
55. Aparici-Robles F, Davidhi A, Carot-Sierra JM et al (2022) Glioblastoma versus solitary brain metastasis: MRI differentiation using the edema perfusion gradient. J Neuroimaging 32:127–133. https://doi.org/10.1111/jon.12920
56. Gates EDH, Weinberg JS, Prabhu SS et al (2021) Estimating local cellular density in glioma using MR imaging data. AJNR Am J Neuroradiol 42:102–108. https://doi.org/10.3174/ajnr.A6884
57. Surov A, Meyer HJ, Wienke A (2017) Correlation between apparent diffusion coefficient (ADC) and cellularity is different in several tumors: a meta-analysis. Oncotarget 8:59492–59499. https://doi.org/10.18632/oncotarget.17752
58. Rahm V, Boxheimer L, Bruehlmeier M et al (2014) Focal changes in diffusivity on apparent diffusion coefficient MR imaging and amino acid uptake on pet do not colocalize in nonenhancing low-grade gliomas. J Nucl Med 55:546–550. https://doi.org/10.2967/jnumed.113.130732
59. Patel KS, Yao J, Raymond C et al (2020) Decorin expression is associated with predictive diffusion MR phenotypes of anti-VEGF efficacy in glioblastoma. Sci Rep 10:14819. https://doi.org/10.1038/s41598-020-71799-w
60. Cindil E, Sendur HN, Cerit MN et al (2021) Validation of combined use of DWI and percentage signal recovery-optimized protocol of DSC-MRI in differentiation of high-grade glioma, metastasis, and lymphoma. Neuroradiology 63:331–342. https://doi.org/10.1007/s00234-020-02522-9
61. Kinoshita M, Uchikoshi M, Tateishi S, et al (2021) Magnetic resonance relaxometry for tumor cell density imaging for glioma: an exploratory study via (11)C-methionine PET and its validation via stereotactic tissue sampling. Cancers (Basel) 13: https://doi.org/10.3390/cancers13164067
62. Bobholz SA, Lowman AK, Brehler M et al (2022) Radio-pathomic maps of cell density identify brain tumor invasion beyond traditional MRI-defined margins. AJNR Am J Neuroradiol 43:682–688. https://doi.org/10.3174/ajnr.A7477
63. Roberts TA, Hyare H, Agliardi G et al (2020) Noninvasive diffusion magnetic resonance imaging of brain tumour cell size for the early detection of therapeutic response. Sci Rep 10:1–13. https://doi.org/10.1038/s41598-020-65956-4
64. Arevalo-Perez J, Thomas AA, Kaley T et al (2015) T1-weighted dynamic contrast-enhanced MRI as a noninvasive biomarker of epidermal growth factor receptor VIII status. Am J Neuroradiol 36:2256–2261. https://doi.org/10.3174/ajnr.A4484
65. Jo SW, Choi SH, Lee EJ et al (2021) Prognostic prediction based on dynamic contrast-enhanced MRI and dynamic susceptibility contrast-enhanced MRI parameters from non-enhancing, T2-high-signal-intensity lesions in patients with glioblastoma. Korean J Radiol 22:1369–1378. https://doi.org/10.3348/kjr.2020.1272
66. Emblem KE, Mouridsen K, Bjornerud A et al (2013) Vessel architectural imaging identifies cancer patient responders to anti-angiogenic therapy. Nat Med 19:1178–1183. https://doi.org/10.1038/nm.3289
67. Boxerman JL, Quarles CC, Hu LS et al (2020) Consensus recommendations for a dynamic susceptibility contrast MRI protocol for use in high-grade gliomas. Neuro Oncol 22:1262–1275. https://doi.org/10.1093/neuonc/noaa141

Authors and Affiliations

Francesco Sanvito[1,2,3] · Catalina Raymond[1,2] · Nicholas S. Cho[1,2,4,5] · Jingwen Yao[1,2] · Akifumi Hagiwara[1,2,6] · Joey Orpilla[7] · Linda M. Liau[7] · Richard G. Everson[7] · Phioanh L. Nghiemphu[8] · Albert Lai[8] · Robert Prins[7] · Noriko Salamon[2] · Timothy F. Cloughesy[8] · Benjamin M. Ellingson[1,2,4,5,7,9]

✉ Benjamin M. Ellingson
bellingson@mednet.ucla.edu

1 UCLA Brain Tumor Imaging Laboratory (BTIL), Center for Computer Vision and Imaging Biomarkers, University of California Los Angeles, 924 Westwood Blvd, Los Angeles, CA 90024, USA

2 Department of Radiological Sciences, David Geffen School of Medicine, University of California Los Angeles, 885 Tiverton Dr, Los Angeles, CA 90095, USA

3 Unit of Radiology, Department of Clinical, Surgical, Diagnostic, and Pediatric Sciences, University of Pavia, Viale Camillo Golgi 19, 27100 Pavia, Italy

4 Medical Scientist Training Program, David Geffen School of Medicine, University of California Los Angeles, 885 Tiverton Dr, Los Angeles, CA 90095, USA

5 Department of Bioengineering, Henry Samueli School of Engineering and Applied Science, University of California Los Angeles, 7400 Boelter Hall, Los Angeles, CA 90095, USA

6 Department of Radiology, Juntendo University School of Medicine, Bunkyo City, 2-Chōme-1-1 Hongō, Tokyo 113-8421, Japan

7 Department of Neurosurgery, David Geffen School of Medicine, University of California Los Angeles, 885 Tiverton Dr, Los Angeles, CA 90095, USA

8 Department of Neurology, David Geffen School of Medicine, University of California Los Angeles, 885 Tiverton Dr, Los Angeles, CA 90095, USA

9 Department of Psychiatry and Biobehavioral Sciences, David Geffen School of Medicine, University of California Los Angeles, 885 Tiverton Dr, Los Angeles, CA 90095, USA